

Cite this: *Chem. Sci.*, 2025, 16, 6050

All publication charges for this article have been paid for by the Royal Society of Chemistry

# Dissecting ionic favorable hydrogen bond chemistry in hybrid separators for aqueous zinc-ion batteries†

Yixiu Wang,<sup>†a</sup> Heng Zhou,<sup>‡a</sup> Shiqiang Wei,<sup>\*a</sup> Hengjie Liu,<sup>a</sup> Shuangming Chen,<sup>†\*a</sup> Xin Chen,<sup>c</sup> Kefu Zhu,<sup>a</sup> Xunshuang Zhang,<sup>a</sup> Yang Si,<sup>a</sup> Xiaojun Wu,<sup>b</sup> Ran Long,<sup>a</sup> Liangbin Li<sup>a</sup> and Li Song<sup>†\*a</sup>

Separators, regulating the ion transport channels between electrodes, are crucial for maintaining the properties of electrochemical batteries. However, sluggish ion transport and desolvation kinetics in aqueous zinc-ion batteries (AZIBs) cause uneven ion flux at the separator–electrode interface, accelerating Zn dendrite growth. Herein, we systematically dissect ionic favorable hydrogen bond chemistry in a hybrid separator engineered through rational boron nitride (BN) doping into polyacrylonitrile (PAN) separators. Notably, *in situ* Fourier transform infrared spectroscopy (FTIR) analyses reveal that the hydrogen bond network in a BN-PAN separator improved the desolvation of Zn<sup>2+</sup> by immobilizing water molecules through hydrogen bond interactions, thus effectively increasing the transference number of zinc ions. Capitalizing on the ionic favorable properties, uniform electric field distribution and zinc plating/stripping behavior are achieved at the separator–electrode interface, efficiently suppressing the formation of zinc dendrites and by-products. As a result, the BN-PAN separator demonstrates extended cycling stability, exceeding 1100 h at a current density of 1.0 mA cm<sup>-2</sup> and 700 h at a current density of 5.0 mA cm<sup>-2</sup>, while exhibiting enhanced rate capability and stability in full cells. This work offers valuable insights into leveraging hydrogen bond chemistry for the design of fast ion-transport separators in aqueous batteries.

Received 21st December 2024  
Accepted 3rd March 2025

DOI: 10.1039/d4sc08624d

rsc.li/chemical-science

## Introduction

The rapid development of large-scale energy conversion and storage technologies has led to a surging demand for high-performance energy storage devices. Lithium-ion batteries, renowned for their high energy density and long cycle life, dominate the global battery market.<sup>1–3</sup> However, the challenges posed by the flammability and toxicity of the electrolytes, coupled with the scarcity of lithium metal resources cannot be ignored.<sup>4,5</sup> Rechargeable aqueous batteries have attracted considerable interest as a promising battery technology due to their intrinsic safety, low cost, and environmental friendliness. Among the various rechargeable aqueous batteries, aqueous

zinc metal batteries have emerged as a promising candidate for large-scale energy storage systems and wearable energy storage devices, owing to their low reduction potential (−0.76 V vs. SHE), high specific capacity (820 mA h g<sup>-1</sup>/5855 mA h cm<sup>-3</sup>) and abundant resources.<sup>6,7</sup> Nevertheless, critical problems occur such as dendrites, corrosion, the hydrogen evolution reaction (HER) and by-products, which cause irreversible degradation of electrochemical performance, thereby hindering their widespread application.<sup>8,9</sup> With the purpose of solving the above problems, researchers have developed numerous optimization strategies focusing on the Zn anode or electrolyte, including anode alloying,<sup>10</sup> electrolyte regulation<sup>11</sup> and solid–electrolyte interphase (SEI) construction,<sup>12</sup> which improve the plating/stripping behavior at the anode surface and mitigate the side reactions to a certain extent.<sup>13–16</sup>

As an important component in direct contact with the cathode, anode and electrolyte, the separator governs the transport environment of zinc ions, which is fundamentally linked to the electrochemical behaviors and safety of the batteries. Problems such as high price, uneven pore structure and the induced dendrite growth of the conventional separators limit their large-scale application, and therefore the design and optimization of the separator–electrolyte and separator–electrode interfaces are of great significance to current research

<sup>a</sup>National Synchrotron Radiation Laboratory, Key Laboratory of Precision and Intelligent Chemistry, University of Science and Technology of China, Hefei 230029, P. R. China. E-mail: sqw@ustc.edu.cn; csm@ustc.edu.cn; song2012@ustc.edu.cn

<sup>b</sup>Hefei National Research Center for Physical Sciences at the Microscale, School of Chemistry and Materials Science, University of Science and Technology of China, Hefei 230026, P. R. China

<sup>c</sup>School of National Defence Science & Technology, Southwest University of Science and Technology, Mianyang 621010, P. R. China

† Electronic supplementary information (ESI) available. See DOI: <https://doi.org/10.1039/d4sc08624d>

‡ These authors contributed equally to this work.



studies.<sup>17</sup> Accordingly, functional modification of separators has emerged as a widely adopted approach.<sup>18–21</sup> However, sluggish ion transport and non-uniform zinc deposition remain challenges limiting the development of AZIBs due to the large solvation structure shell of  $[\text{Zn}(\text{H}_2\text{O})_6]^{2+}$  and poor interfacial charge transfer kinetics.<sup>22</sup> Various effective methods have been extensively developed to enhance the ion transport process within separators, including engineering uniform ion transport channels with controlled porosity,<sup>23,24</sup> improving ion selective permeability through electrostatic interaction,<sup>25</sup> facilitating rapid zinc ion capture and transport with incorporated zincophilic materials,<sup>26,27</sup> and modulating  $\text{SO}_4^{2-}$  and  $\text{H}_2\text{O}$  transport behavior with intermolecular interactions, predominantly hydrogen bond chemistry.<sup>28–30</sup> Significantly, hydrogen bond chemistry is a promising strategy for achieving high-performance AZIBs based on the electrolyte properties.<sup>31</sup> Separators functionalized with oxygen-containing groups or hydrogen bond networks have been designed and utilized to immobilize water molecules through hydrogen bond interactions, thereby simultaneously facilitating the desolvation process of zinc ions and suppressing water-induced side reactions.<sup>21,32–34</sup> Despite these advances, there is still a lack of clear understanding of the dynamic evolution of hydrogen bond networks in promoting ion transport. Hence, it is essential to develop an appropriate research object to dissect the hydrogen bond chemistry in AZIB separators and elucidate the dynamic ion transport mechanism at the molecule level with advanced *in situ* techniques.

Herein, we selected polyacrylonitrile (PAN) as the study object of separators and introduced boron nitride (BN) as inorganic particles to construct hybrid separator materials with a hydrogen bond network. The dynamic investigation of zinc ion transport through separators was carried out *via in situ* Fourier transform infrared spectroscopy (FTIR). The results demonstrated that the strong hydrogen bond interactions favored the desolvation process by anchoring the water molecules and enhanced selective permeability of zinc ions. Moreover, the BN-PAN separator enabled a homogeneous electric field distribution and orderly ion migration at the separator–electrode interface, thereby promoting uniform zinc deposition and simultaneously suppressing side reactions. As a result, the Zn/BN-PAN/Zn symmetric cell exhibited remarkable stability, achieving a long cycle life of 1100 h at a current density of  $1.0 \text{ mA cm}^{-2}$  and a capacity of  $1.0 \text{ mA h cm}^{-2}$ , and 700 h at a current density of  $5.0 \text{ mA cm}^{-2}$  and a capacity of  $5.0 \text{ mA h cm}^{-2}$ . Meanwhile, the BN-PAN separators also attained synergistic improvements in capacity, rate performance and cycle stability for full batteries, indicating their potential for application in various advanced electrochemical energy storage devices.

## Results and discussion

BN-PAN inorganic–organic hybrid separators were prepared using a non-solvent thermal phase separation method, together with the blade coating method (Fig. 1a). The successful synthesis of BN-PAN separators was confirmed by the X-ray diffraction (XRD) analysis (Fig. S1†), where characteristic (100)

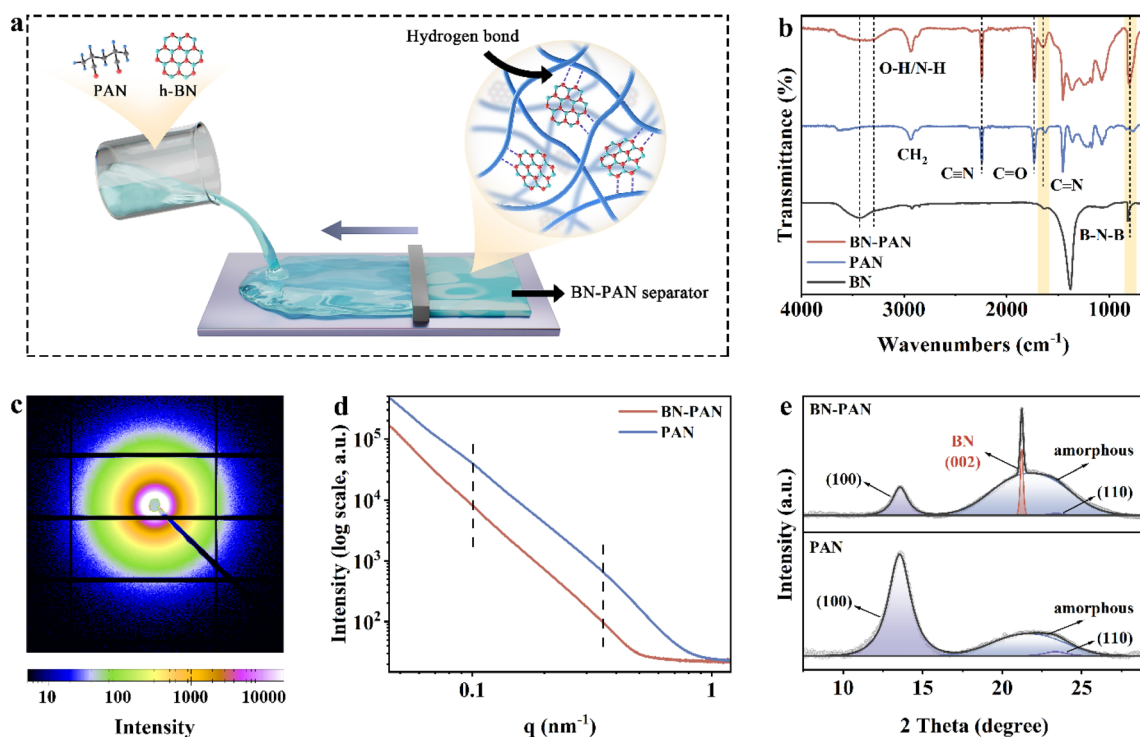


Fig. 1 Structural characterization of BN-PAN and PAN separators. (a) The synthetic process of the BN-PAN separator. (b) The FTIR spectra of the BN-PAN separator, the PAN separator and BN. (c) 2D SR-SAXS pattern of the BN-PAN separator. (d) Corresponding 1D integrated curves of the 2D SR-SAXS patterns of the BN-PAN separator and PAN separator. (e) Multiplex fitting of the 1D integrated WAXS curve of the BN-PAN separator and PAN separator.



and (110) peaks from PAN and the (002) peak from BN were observed. The morphology, thickness and elemental distribution of the separators were characterized by scanning electron microscopy (SEM) measurement (Fig. S2–S4†). The surface of a pure PAN separator showed localized depressions and broken holes, whereas the BN-PAN separator displayed a more uniform and complete porosity distribution, suggesting that BN contributed to optimizing the film forming process of PAN. The SEM cross-sectional images and the corresponding EDS-mapping images revealed a thickness of 170  $\mu\text{m}$  for the BN-PAN separator, with a homogeneous distribution of B, N, and C elements, proving the uniform dispersion of BN within the PAN matrix.

Fourier transform infrared spectroscopy (FTIR) was employed to investigate the functional group structure and the hydrogen bond interactions of the separators (Fig. 1b). The FTIR results showed that the peaks near 2940  $\text{cm}^{-1}$ , 2243  $\text{cm}^{-1}$  and 819  $\text{cm}^{-1}$  correspond to the stretching vibration of the C–H bond in the PAN polymer chain, the stretching vibration of the C $\equiv$ N bond, and the bending vibration of the B–N–B bond, respectively.<sup>35</sup> In addition, the stretching vibration peak of the C=N bond near 1650  $\text{cm}^{-1}$  was greatly enhanced in the BN-PAN separator,<sup>36</sup> implying that BN doping promotes the decomposition of the –C $\equiv$ N bond, thereby increasing the content of the –C=N–H bond. More importantly, in comparison to the FTIR spectra of pure PAN and BN, both the C=N bond and B–N bond exhibited a significant shift in the BN-PAN spectra, indicating the existence of hydrogen bonds between the BN inorganic particles and the PAN polymer.<sup>37,38</sup> The stretching vibration of O–H/N–H bonds in the BN-PAN spectra appeared near 3500–3200  $\text{cm}^{-1}$  with a significant broadening, which also suggested the presence of strong hydrogen bond interactions in the chain network of the BN-PAN polymer.<sup>39</sup> Such interactions with the polymer matrix can effectively avoid the detachment of inorganic particles during battery cycling and maintain the homogeneity and integrity of the modified separator, promoting stable ion migration. In addition, the hydrophilic functional –OH and –NH groups in the BN-PAN separator resulted in a smaller contact angle of 2 M ZnSO<sub>4</sub> electrolyte on its surface (Fig. S5†), reflecting better electrolyte permeability due to BN doping.<sup>40</sup> The thermogravimetric analysis (TGA) also proved that the thermal stability of the separator was improved after doping BN (Fig. S6†).

Synchrotron radiation small-angle X-ray scattering (SR-SAXS) and wide-angle X-ray scattering (SR-WAXS) tests were carried out on BN-PAN and PAN separators to investigate the effect of BN doping on the microstructure. SR-SAXS analysis focuses on the scattering in the small-angle range, and probes the periodic structure of the polymer within the range from 1 nm to 100 nm.<sup>41</sup> The results of SR-SAXS (Fig. 1c, d and S7†) illustrated the presence of weak scattering peaks at  $q = 0.10 \text{ nm}^{-1}$  and  $q = 0.35 \text{ nm}^{-1}$  in the PAN separator, while none were observed in the BN-PAN separator, demonstrating that BN doping further reduced the degree of structural order in the PAN polymer.<sup>42</sup> SR-WAXS tests covering a wide angular range (5–70°) were further utilized to compare the crystallinity of the separators. Fig. 1e shows the one-dimensional integrated WAXS curves and the

results of multiplex fitting. After BN doping, no additional scattering peaks were observed except for the emergence of the (002) crystalline peak from BN, while the (100) and (110) crystalline peaks of PAN were preserved, indicating that the addition of BN did not alter the type of crystal structure of PAN. However, a notable reduction in the intensity of the (100) and (110) crystalline peaks was detected in the BN-PAN separator, accompanied by a corresponding increase in the intensity of the amorphous peak. Further calculation of the crystallinity in PAN by Gaussian fitting revealed that the crystallinity of the PAN polymer decreased dramatically from 64.9% to 16.0% with the addition of BN. The integrated analysis of SR-SAXS and SR-WAXS results concludes that BN doping significantly reduced the crystallinity and the degree of structural order in the PAN polymer. It is noteworthy that the ionic conductivity of polymers is closely related to their crystallinity.<sup>43</sup> To elucidate this correlation, the ionic conductivity of BN-PAN and PAN separators was evaluated using electrochemical impedance spectroscopy (EIS) as shown in Fig. S8.† The results presented that the ionic conductivity of the BN-PAN separator (11.02  $\text{mS cm}^{-1}$ ) is substantially higher than that of the PAN separator (5.21  $\text{mS cm}^{-1}$ ), which is beneficial for the accelerated transport of zinc ions. In brief, the doped BN inorganic particles were proven to be capable of disrupting the crystalline regions of PAN and increasing the proportion of amorphous regions, consequently introducing more free volume space. This phenomenon enhanced the ionic conductivity of the PAN separator and facilitated the migration of zinc ions.<sup>44,45</sup> Additionally, the results of nitrogen absorption/desorption isotherms revealed that the pore size of the PAN separator increased from 18.88 nm to 22.18 nm after doping BN, which is advantageous for broadening the transport channel of zinc ions (Fig. S9†).

The enhanced ionic conductivity based on reduced structural order and the hydrogen bond network achieved in the BN-doped PAN separator provided prior conditions for promoting the transport of zinc ions. But it still requires in-depth investigation on the facilitation and modulation mechanism of zinc ion transport during the energy storage process. Thus, *in situ* FTIR, *ex situ* X-ray absorption near-edge structure (XANES) and X-ray photoelectron spectroscopy (XPS) measurements were employed. *In situ* FTIR measurements were conducted in ATR mode using the device illustrated in Fig. 2a. An infrared beam was directed through a silicon crystal to reach the sample, where Ti mesh and zinc foil served as the cathode and anode, respectively, with a BN-PAN or PAN membrane as the separator. The initial infrared spectrum was collected as the background, and subsequent spectra were processed to obtain the corresponding operational signals, which enabled clear visualization of changes in hydrogen bond interactions during charging and discharging processes. *In situ* FTIR spectroscopy of a Zn//Ti cell with the BN-PAN separator revealed that the stretching vibration peaks of the O–H/N–H bonds exhibited a blue-shift, increased intensity and significant broadening (Fig. 2b), while the cell using the PAN separator displayed only a slight enhancement in the O–H/N–H bond vibrations without a noticeable shift (Fig. 2c and S10†). These results demonstrate the formation of hydrogen bonds with water molecules in the



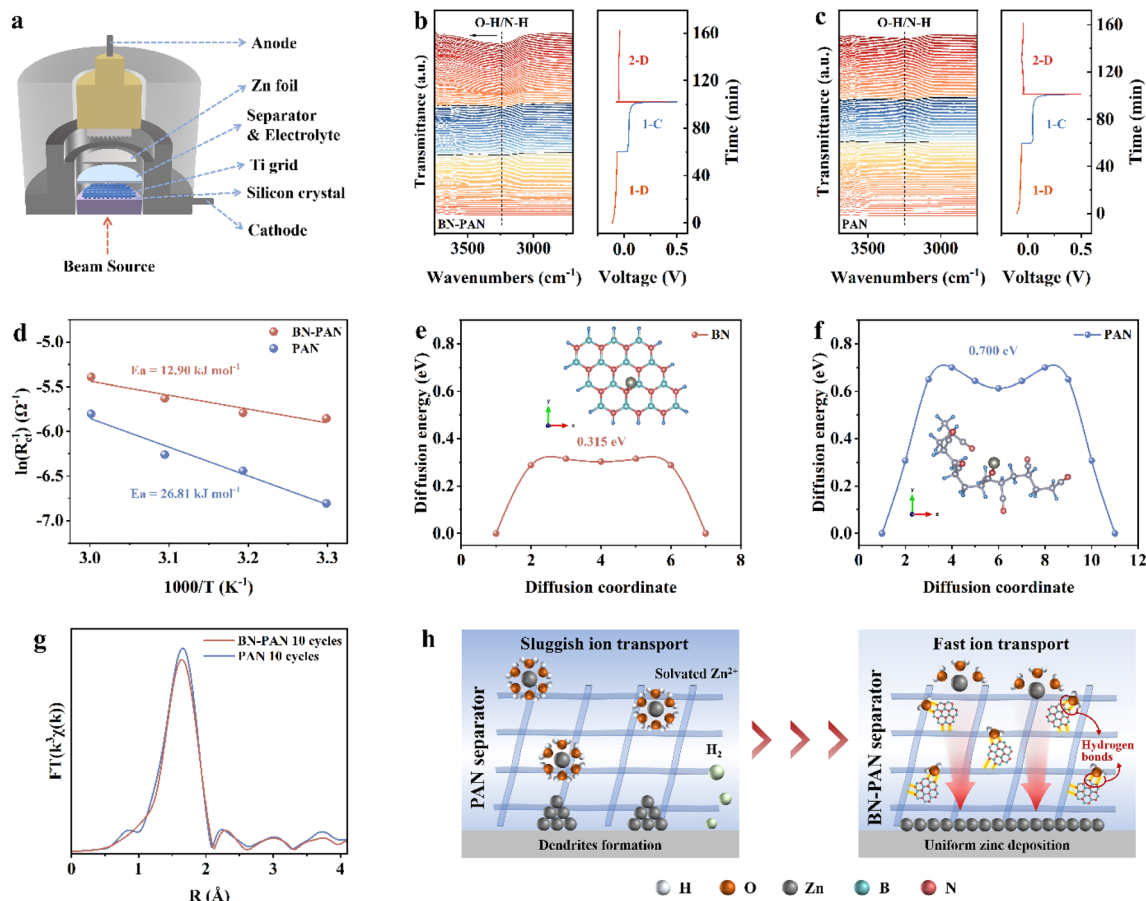


Fig. 2  $\text{Zn}^{2+}$  transport mechanism of BN-PAN and PAN separators. (a) Schematic diagram of the device for the *in situ* FTIR test. *In situ* FTIR spectroscopy of Zn/Ti cells with the (b) BN-PAN separator and (c) PAN separator. (d) The comparison of activation energies of BN-PAN and PAN separators. The migration energy barrier of  $\text{Zn}^{2+}$  on (e) BN and (f) PAN. (g) Fourier-transformed Zn K-edge EXAFS spectra of BN-PAN and PAN separators after 10 cycles. (h) Schematic illustration of the  $\text{Zn}^{2+}$  transport mechanism with BN-PAN and PAN separators.

BN-PAN separator during cycling, which consequently weakens the interactions between the water molecules and zinc ions, thereby accelerating the desolvation process.<sup>46</sup> The temperature-dependent EIS study was carried out to further investigate the desolvation effect (Fig. S11†), and the activation energy ( $E_a$ ) was calculated according to the Arrhenius equation (Fig. 2d). Compared to using the PAN separator (26.81  $\text{kJ mol}^{-1}$ ), the cell with the BN-PAN separator had lower  $E_a$  (12.90  $\text{kJ mol}^{-1}$ ), proving that the BN-PAN separator can effectively promote the desolvation process of zinc ions *via* hydrogen bond networks, which led to fast ion transfer.<sup>47</sup>

To further clarify the specific role of BN as a dopant in the separators, the XPS spectra of the BN-PAN and PAN separators after immersion in 2 M  $\text{ZnSO}_4$  electrolyte were analyzed. It can be seen in Fig. S12† that the peaks at 1044.9 eV and 1021.9 eV of the Zn 2p spectrum were ascribed to the typical electronic states of Zn 2p<sub>3/2</sub> and Zn 2p<sub>1/2</sub>. In comparison to pure  $\text{ZnSO}_4$ , the BN-PAN and PAN separators displayed a negative shift of 0.38 eV and 0.43 eV, respectively, in the Zn 2p spectrum after absorption. Besides, the N 1s spectrum revealed a positive shift of the -CN peak in the BN-PAN (0.14 eV) and PAN (0.26 eV) separators after absorption (Fig. S13†). This shift can be attributed to the

electron transfer between N and Zn, which means a pure PAN polymer with -CN functional groups can form electrostatic interaction with  $\text{Zn}^{2+}$  and promote the orderly shuttling of zinc ions,<sup>48</sup> proving to be a suitable matrix material for separators in AZIBs. Notably, a greater positive shift (0.46 eV) was observed in the B 1s spectrum of the BN-PAN separator after absorption, implying that electron transfer also occurred between B and Zn, further optimizing the ordered migration process of zinc ions (Fig. S14†). The transport behavior of zinc ions on the surface of BN and PAN was simulated by using ORCA version 5.0.2 for density functional theory (DFT) calculations for further illustrating the effect of BN on zinc ion migration.<sup>49–51</sup> For the calculations of the  $\text{Zn}^{2+}$  migration energy barriers, there was only one imaginary frequency in the results of the frequency calculations, indicating that a transition state was indeed identified (Tables S1 and S2†). The results showed that zinc ions achieved lower migration energy barriers on the BN surface compared to that of PAN (Fig. 2e and f), which revealed that BN effectively promoted the migration process of zinc ions. The Zn K-edge XANES analysis of the separators after cycling was conducted to further investigate the facilitation mechanism of zinc ion transport in the BN-PAN separators (Fig. S15†). Compared to



the PAN separator, the absorption edge of the BN-PAN separator after cycling shifted to higher energy, showing a reduction in the electrons surrounding Zn. The Fourier-transformed Zn K-edge EXAFS spectra of *R* space (Fig. 2g) presented a decrease in the Zn–N/O bond length for the BN-PAN separator after cycling, which was consistent with the calculation results for the structure of BN and PAN after the absorption of zinc ions (Table S3†). This decrease can be attributed to the strong interaction between the BN-PAN separator and zinc ions. These findings comprehensively illustrated that the doping of BN enabled the ionic favorable hydrogen bond network and optimized the separator–electrolyte interfacial interaction, improving the desolvation process and the ion transport kinetics. The shorter Zn–N/O bond length suggested that a sufficient interaction existed between the separator and the zinc ions for guiding ordered ion transport, while the smaller adsorption and diffusion energy barriers of zinc ions indicated fast migration of zinc ions favored by BN-doping, achieving an enhanced ion transport process. As a result, the BN-PAN separator attained a higher Zn<sup>2+</sup> transference number ( $t_{\text{Zn}^{2+}}$ ) of 0.595 than that of the PAN separator (0.491) (Fig. S16†). In addition, the ion selectivity of the separators was evaluated using H-cells (Fig. S17†). Inductively coupled plasma (ICP) was used to quantify the elemental content on the water side after a 2 h standing period. The results showed that the BN-PAN separator offered a higher Zn/S transmission ratio, confirming its ability to selectively transport Zn<sup>2+</sup> while impeding the transfer of SO<sub>4</sub><sup>2−</sup> (Fig. S18†). These phenomena further substantiated that the BN-PAN separator modulated the solvation shell of Zn<sup>2+</sup> via the hydrogen bond network and optimized the interfacial interaction with zinc ions, thereby promoting efficient migration of zinc ions (Fig. 2h).

In order to investigate the effect of the optimized zinc ion transport at the separator–electrode interface, *in situ* optical microscopy, SEM and XRD characterization studies were conducted to observe zinc plating/stripping behavior. Firstly, the zinc plating process on the surface of the Zn anode at a current of 5 mA was observed using an *in situ* optical microscope (Fig. 3a). When the PAN separator was employed, the zinc deposition on the surface of the Zn anode was uneven and irregular. Localized protrusions emerged after 60 min of deposition and evolved into dendritic structures after 90 min. In contrast, when the BN-PAN separator was utilized, the zinc deposition on the surface of the Zn anode was more uniform and flat with no localized protrusion observed after 90 minutes. Secondly, the SEM image of the Zn anode surface after 10 cycles with the BN-PAN separator illustrated the uniform and dense deposition morphology (Fig. 3b). Conversely, the surface of the Zn anode cycled with the PAN separator exhibited flake-like zinc depositions of different sizes and irregular distribution (Fig. 3c and S19†). These findings suggest that the BN-PAN separator can effectively regulate the plating behavior of the Zn anode, which is helpful for improving cycle stability. Thirdly, the XRD patterns (Fig. S20†) of the Zn anodes after cycling revealed that the intensity of the (002) peak of the Zn anode cycled with the BN-PAN separator was higher than that of the Zn anode cycled with the PAN separator. Previous studies have proposed that Zn

tends to deposit unevenly on the (100) and (101) crystal facets, which in turn leads to the formation of protrusions and dendrites. On the other hand, Zn tends to grow along a horizontal direction, forming a uniform flat deposition on the (002) crystal facet.<sup>21,52,53</sup> Consequently, the XRD results further demonstrate that the BN-PAN separator can promote uniform zinc deposition, thereby stabilizing the Zn anode. In addition, the distinct peak at 8.0° was attributed to the formation of by-products (Zn(OH)<sub>2</sub>)<sub>3</sub>(ZnSO<sub>4</sub>)(H<sub>2</sub>O)<sub>5</sub> (PDF#78-0246), which exhibited lower intensity for the zinc anode with the BN-PAN separator than that of the PAN separator, suggesting that the BN-PAN separator could inhibit side reactions. To further illustrate the enhancement of ion transport induced by hydrogen bond interactions, the EIS spectra after 10 cycles of Zn//Zn cells were tested, which showed that the ion transfer process in BN-PAN was still faster than that in PAN after multiple cycles, demonstrating that the improved ion transport was not originated from the formation of the SEI in the first cycle (Fig. S21†). Furthermore, the SEM images of the BN-PAN separator after cycling exhibited a complete and uniform pore structure, indicating its superior chemical durability (Fig. S22†).

The electric field distribution in zinc symmetric cells was simulated using finite element analysis (FEA) of COMSOL. The results showed that the electric field distribution on the surface of the zinc anode with the PAN separator was non-uniform and tended to concentrate on the dendrite seeds, thereby exacerbating dendrite growth (Fig. 3e). In contrast, the BN-PAN separator led to a more uniform electric field distribution on the surface of the zinc anode, mitigating charge accumulation and suppressing dendrite formation (Fig. 3d). Moreover, zinc nucleation and deposition were further investigated using the amperometric *i*–*t* curve tests at a constant potential (Fig. 3f). The current density increased persistently with time in Zn/PAN/Zn cells, meaning that the Zn anode surface underwent a continuous two-dimensional (2D) diffusion, which led to Zn aggregation and exacerbated the growth of Zn dendrites.<sup>54</sup> Instead, the Zn/BN-PAN/Zn cell presented a short 2D diffusion time followed by a stable three-dimensional (3D) diffusion with a constant current density, inferring that Zn<sup>2+</sup> ions absorbed at the surface appeared to be locally reduced to Zn<sup>0</sup> under restricted 2D surface diffusion conditions. The lower 2D diffusion currents with the BN-PAN separator implied an additional energy barrier for absorbed zinc ions to migrate laterally, consequently forcing them to deposit close to the initial absorption site. The number of nucleation sites increased, favoring the formation of small-sized, dense nucleus seeds and ultimately resulting in a homogeneous and dense zinc deposition layer.<sup>55,56</sup> Therefore, the BN-PAN separator achieved accelerated ion transport through a hydrogen bond network in parallel with the regulation of the zinc plating/stripping behavior and the charge distribution at the separator–electrode interface, creating a stable ion transport environment.

A series of electrochemical tests were employed to explore the influence of doping BN on the inhibition of side effects. The linear sweep voltammetry (LSV) curves (Fig. S23†) displayed a distinct hysteresis of the hydrogen evolution reaction (HER) and oxygen evolution reaction (OER) potential in the Zn//Cu



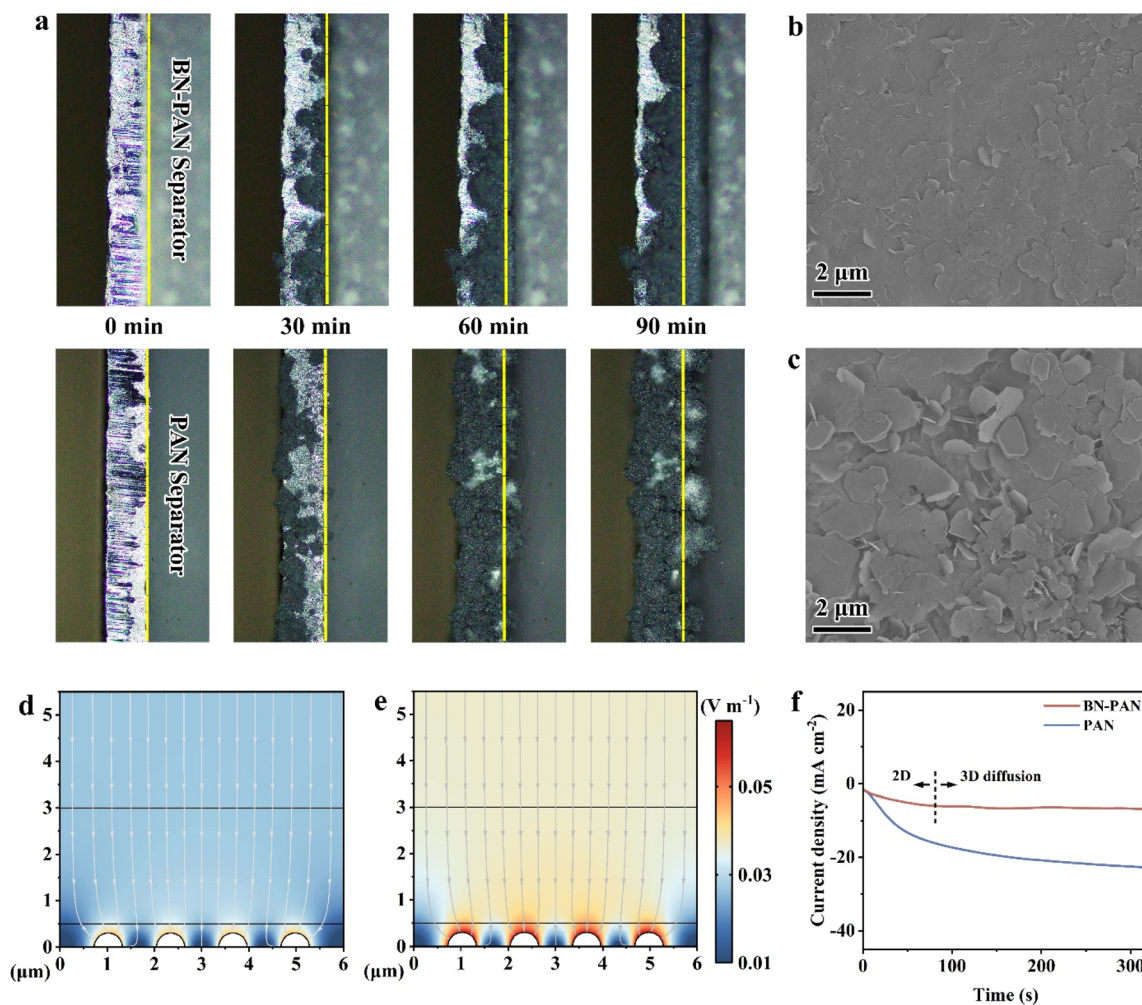


Fig. 3 The Zn plating/stripping process in Zn//Zn cells. (a) *In situ* optical microscope images of Zn plating/stripping at 5 mA for Zn anodes with the use of BN-PAN and PAN separators. The SEM images of the Zn anode surface after 10 cycles with the (b) BN-PAN separator and (c) PAN separator. The electrical field models based on the (d) BN-PAN separator and (e) PAN separator. (f) The amperometric  $i-t$  curves of Zn//Zn cells with BN-PAN and PAN separators at an overpotential of  $-150$  mV.

cells with BN-PAN separators compared to those with PAN separators. The results imply that the BN-PAN separator can effectively expand the electrochemical reaction window of the battery, enhance the electrochemical stability,<sup>57</sup> and simultaneously suppress the HER on the Zn anode. In addition, the suppression of the corrosion reaction on the zinc anode by using the BN-PAN separator was evidenced by the Tafel test (Fig. S24<sup>†</sup>). Higher corrosion potentials and lower corrosion current densities represent reduced corrosion reaction potential and decreased corrosion rates, respectively.<sup>58,59</sup> The doping of BN in the PAN separator led to an increased corrosion potential and a decreased corrosion current for the Zn anode, indicating that the BN-PAN separator can mitigate the propensity for corrosion and the HER. In short, BN-PAN separators can suppress the side reactions and thus improve the stability of the batteries.

To investigate the electrochemical performance of BN-PAN separators, Zn//Zn and Zn//Cu cells were assembled for electrochemical characterization. The Zn/BN-PAN/Cu cell exhibited lower voltage polarization compared to the Zn/PAN/Cu cell and Zn/glass fiber/Cu cell, indicating improved reversibility of zinc

plating/stripping with the use of the BN-PAN separator (Fig. S25<sup>†</sup>). In the coulombic efficiency test (Fig. S26<sup>†</sup>), the Zn/BN-PAN/Cu cell maintained a stable CE value for over 300 cycles, whereas the Zn/PAN/Cu cell and Zn/glass fiber/Cu cell could only sustain stability for 135 cycles and 51 cycles, respectively. The cycling stability of BN-PAN, PAN and glass fiber separators was evaluated at different current densities. The Zn/BN-PAN/Zn cells attained ultra-long cycle life (1100 h) at a current density of  $1.0 \text{ mA cm}^{-2}$  and a capacity of  $1.0 \text{ mA h cm}^{-2}$  (Fig. 4a). In contrast, the Zn/PAN/Zn cell and Zn/glass fiber/Zn cell experienced short circuit at 93 h and 60 h, respectively. When the current density and capacity were further increased to  $5.0 \text{ mA cm}^{-2}$  and  $5.0 \text{ mA h cm}^{-2}$ , the Zn/BN-PAN/Zn cell enabled stable cycling for over 700 h, while the Zn/PAN/Zn cell and Zn/glass fiber/Zn cell encountered a short circuit at 57 h and 53 h, respectively (Fig. 4b and S27<sup>†</sup>). Compared with recent research studies on modified separators for AZIBs, the BN-PAN separator showed a superior cycling life (Fig. 4c and Table S4<sup>†</sup>).

In order to assess the feasibility of the BN-PAN separators in practical applications, full cells were fabricated by coupling the



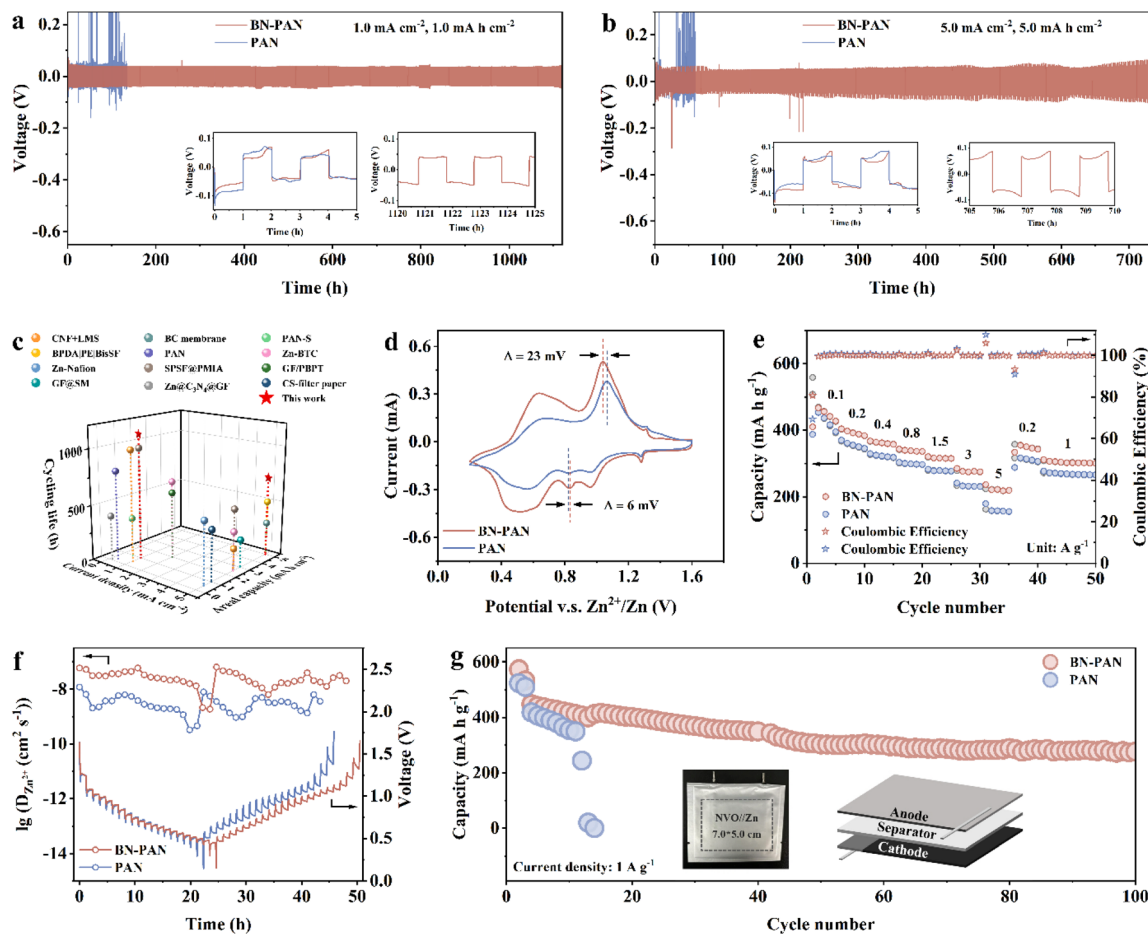


Fig. 4 Electrochemical performance of BN-PAN and PAN separators. The cycling performance of Zn//Zn cells at (a)  $1.0 \text{ mA cm}^{-2}$  with  $1.0 \text{ mA h cm}^{-2}$  and (b)  $5.0 \text{ mA cm}^{-2}$  with  $5.0 \text{ mA h cm}^{-2}$  using the BN-PAN separator and PAN separator. (c) The comparison among our BN-PAN separator and previous reports. (d) The CV curves at a scan rate of  $0.2 \text{ mV s}^{-1}$ , (e) the rate performance at a current density from  $0.1 \text{ A g}^{-1}$  to  $5.0 \text{ A g}^{-1}$ , (f) the charge–discharge GITT curves at a current density of  $0.1 \text{ A g}^{-1}$  and the corresponding  $\text{Zn}^{2+}$  coefficients of Zn//NVO full cells, and (g) the cycling stability of pouch cells at a current density of  $1.0 \text{ A g}^{-1}$ .

separators with the ammonium-intercalated vanadium oxide (NVO) cathode (Fig. S28<sup>†</sup>). The cyclic voltammetry (CV) plots in Fig. 4d showed that the voltage gap of redox peaks in the Zn/BN-PAN/NVO cell was reduced by approximately 29 mV in comparison with that of the Zn/PAN/NVO cell, which is consistent with the diminished voltage polarization in the GCD curves (Fig. S29<sup>†</sup>). Likewise, the electrochemical impedance spectroscopy (EIS) results also evidenced that the Zn/BN-PAN/NVO cells had lower charge-transfer resistance than the Zn/PAN/NVO cells, both before and after cycling (Fig. S30<sup>†</sup>). These results jointly demonstrated that the BN-PAN separator improved the electrochemical reversibility and reaction kinetics of AZIBs. Benefiting from the comprehensive modulation effect of the BN-PAN separator, the Zn/BN-PAN/NVO cells realized higher capacity and superior rate performance (Fig. 4e). At a current density of  $0.1 \text{ A g}^{-1}$ , the Zn/BN-PAN/NVO cell delivered a capacity of up to  $440.26 \text{ mA h g}^{-1}$ . As the current density was increased to  $5.0 \text{ A g}^{-1}$ , the Zn/BN-PAN/NVO cell maintained a high capacity of  $223.74 \text{ mA h g}^{-1}$ , representing a 38.3% improvement over that of the Zn/PAN/NVO cell. It is worth noting that the Zn/BN-PAN/NVO cell exhibited a capacity

retention of 50.8% when the current density was increased by a factor of 50, surpassing that of the Zn/PAN/NVO cell (38.7%). Additionally, the Zn/BN-PAN/NVO cell achieved better cycle stability than the Zn/PAN/NVO cell at a current density of  $5 \text{ A g}^{-1}$  with different N/P ratios (Fig. S31, S32 and Table S5<sup>†</sup>). To further verify the ability of BN-PAN separators to promote zinc ion transport in full cells, the zinc ion diffusion coefficient ( $D_{\text{Zn}^{2+}}$ ) was determined using the galvanostatic intermittent titration technique (GITT) (Fig. 4f). The results revealed that the Zn/BN-PAN/NVO cell possessed a higher  $D_{\text{Zn}^{2+}}$  ( $10^{-8}$  to  $10^{-9} \text{ cm}^2 \text{ s}^{-1}$ ) compared to the Zn/PAN/NVO cell ( $10^{-8}$  to  $10^{-10} \text{ cm}^2 \text{ s}^{-1}$ ). The practicality of the BN-PAN separator was also verified in pouch cells with a size of  $7 \times 5 \text{ cm}$  (Fig. 4g). The pouch cell with the BN-PAN separator achieved improved capacity and stability performance than that with the PAN separator. At a current density of  $1 \text{ A g}^{-1}$ , the Zn//BN-PAN//NVO pouch cell enabled remarkable stability for 100 cycles and a capacity retention of  $\sim 70\%$  after 60 cycles. For further verification of the applicability of the BN-PAN separator, the electrochemical performance in Zn–I<sub>2</sub> batteries was measured. The Zn–I<sub>2</sub> batteries with the BN-PAN separator exhibited improved rate capacity than that with



the PAN separator (Fig. S33†). When using the BN-PAN separator, the Zn-I<sub>2</sub> battery provided a high capacity of 178.0 mA h g<sup>-1</sup> at a current density of 0.2 A g<sup>-1</sup> and maintained a capacity of up to 121.2 mA h g<sup>-1</sup> at a current density of 5.0 A g<sup>-1</sup>, which were better than that of the Zn-I<sub>2</sub> battery with the PAN separator (153.0 mA h g<sup>-1</sup> at 0.2 A g<sup>-1</sup> and 105.2 mA h g<sup>-1</sup> at 5.0 A g<sup>-1</sup>). In addition, the Zn-I<sub>2</sub> battery with the BN-PAN separator showed a stable cycling performance with a capacity retention of 90.0% after 3000 cycles at a current density of 5 A g<sup>-1</sup>. In contrary, the Zn-I<sub>2</sub> battery with the PAN separator exhibited lower capacity with a capacity retention of 82.4% after 3000 cycles (Fig. S34†). In conclusion, the BN-PAN separator has been proven to be practical in the Zn-I<sub>2</sub> battery with enhanced capacity, rate and cycling performance. According to the literature, among the recently reported separator materials, the BN-PAN separator provided better capability in full cells with vanadium-based cathodes, as well as in Zn-I<sub>2</sub> batteries (Table S6†). To sum up, the BN-doped PAN separator can enhance the transport kinetics of zinc ions, improve the reversibility and stability of the zinc plating/stripping process, and thus achieve a synergistic improvement of the capacity, rate performance and cycling stability for AZIBs.

## Conclusions

In conclusion, we introduced hydrogen bond chemistry *via* BN-doping in PAN separators and conducted an in-depth study on the internal ion transport mechanism. Synchrotron X-ray scattering and FTIR analyses revealed that the BN modifier endowed the separator with increased amorphous regions and enhanced hydrogen bond interactions, realizing increased ionic conductivity. In particular, *in situ* FTIR measurement was employed for dissecting the hydrogen bond evolution during the cycling process, which illustrated that the ionic favorable hydrogen bond network within the BN-PAN separator optimized the solvation structure of zinc ions through selective water molecule immobilization, thereby facilitating zinc ion transport. Additionally, the strong interaction between B and Zn improved the orderly migration of zinc ions, contributing to uniform zinc deposition and a reduced migration energy barrier, as observed through *in situ* optical microscopy and DFT calculations. Benefiting from the synergistic effect of the BN-PAN separator on the efficiency and uniformity of zinc ion transport, the zinc symmetric battery exhibited stable cycling performance (1100 h at 1.0 mA cm<sup>-2</sup> for 1.0 mA h cm<sup>-2</sup> and 700 h at 5.0 mA cm<sup>-2</sup> for 5.0 mA h cm<sup>-2</sup>). The practicality of the BN-PAN separator was verified by the great improvement in the performance of full cells, with a capacity enhancement to 440.26 mA h g<sup>-1</sup> at a current density of 0.1 A g<sup>-1</sup>. This study provides new insights for elucidating the underlying ion transport mechanisms facilitated by hydrogen bond chemistry at the molecule level.

## Data availability

The data supporting this article have been included as part of the ESI.†

## Author contributions

L. S., S. C. and S. W. supervised the project. Y. W. carried out most of the experiments and data analysis. H. Z. and X. W. performed the DFT calculations. H. L. helped carry out the *in situ* FTIR measurements. X. C., X. Z. and L. L. provided useful preparation methods for polymer materials. Y. S. and K. Z. helped perform some sample characterization studies. R. L. provided assistance in COMSOL simulation. All authors discussed the results and commented on this manuscript.

## Conflicts of interest

There are no conflicts to declare.

## Acknowledgements

This work was financially supported in part by the National Key R&D Program of China (2020YFA0405800), the NSFC (12225508, 12322515, U23A20121, and 12205301), the Youth Innovation Promotion Association of CAS (2022457), the China Post-doctoral Science Foundation (BX20230346 and 2023M743365), the Anhui Provincial Natural Science Foundation (2408085QA004), and the Fundamental Research Funds for the Central Universities (WK2060000039 and WK2060000099). We thank the Shanghai Synchrotron Radiation Facility (BL10U1 and BL14W1), the Hefei Synchrotron Radiation Facility (infrared spectroscopy and microspectroscopy, MCD-A and MCD-B), and the USTC Center for Micro and Nanoscale Research and Fabrication for helps in characterization. This work was partially carried out at the Instruments Center for Physical Science, University of Science and Technology of China. We thank Dr Chengming Wang for his kind help in ATR-IR tests and analyses.

## Notes and references

- 1 K. Kang, Y. S. Meng, J. Bréger, C. P. Grey and G. Ceder, Electrodes with High Power and High Capacity for Rechargeable Lithium Batteries, *Science*, 2006, **311**, 977–980.
- 2 J. B. Goodenough and K.-S. Park, The Li-Ion Rechargeable Battery: A Perspective, *J. Am. Chem. Soc.*, 2013, **135**, 1167–1176.
- 3 J. He, C. Lu, H. Jiang, F. Han, X. Shi, J. Wu, L. Wang, T. Chen, J. Wang, Y. Zhang, H. Yang, G. Zhang, X. Sun, B. Wang, P. Chen, Y. Wang, Y. Xia and H. Peng, Scalable production of high-performing woven lithium-ion fibre batteries, *Nature*, 2021, **597**, 57–63.
- 4 B. Liu, Y. Jia, C. Yuan, L. Wang, X. Gao, S. Yin and J. Xu, Safety issues and mechanisms of lithium-ion battery cell upon mechanical abusive loading: a review, *Energy Storage Mater.*, 2020, **24**, 85–112.
- 5 S. Chen, F. Dai and M. Cai, Opportunities and Challenges of High-Energy Lithium Metal Batteries for Electric Vehicle Applications, *ACS Energy Lett.*, 2020, **5**, 3140–3151.
- 6 H. Li, L. Ma, C. Han, Z. Wang, Z. Liu, Z. Tang and C. Zhi, Advanced rechargeable zinc-based batteries: recent





- Biomass Bamboo Membrane Separator, *Adv. Mater.*, 2024, **36**, 2406429.
- 34 Y. Yuan, J. Yang, Z. Liu, R. Tan, M. Chuai, J. Sun, Y. Xu, X. Zheng, M. Wang, T. Ahmad, N. Chen, Z. Zhu, K. Li and W. Chen, A Proton-Barrier Separator Induced *via* Hofmeister Effect for High-Performance Electrolytic MnO<sub>2</sub>-Zn Batteries, *Adv. Energy Mater.*, 2022, **12**, 2103705.
- 35 M. K. Haider, A. Ullah, M. N. Sarwar, T. Yamaguchi, Q. Wang, S. Ullah, S. Park and I. S. Kim, Fabricating Antibacterial and Antioxidant Electrospun Hydrophilic Polyacrylonitrile Nanofibers Loaded with AgNPs by Lignin-Induced *In Situ* Method, *Polymers*, 2021, **13**, 748.
- 36 X. Chen, C. Wan, R. Yu, L. Meng, D. Wang, T. Duan and L. Li, Fabrication of amidoximated polyacrylonitrile nanofibrous membrane by simultaneously biaxial stretching for uranium extraction from seawater, *Desalination*, 2020, **486**, 114447.
- 37 J. Li, Y. Zhu, R. Bian, Y. Wei, S. Jiang, K. Li, X. Li, D. Tian, X. Zhan and J. Li, Construction of a boron nitride nanosheet hybrid for tough, strong, and flame-retardant phenolic resins, *Chem. Eng. J.*, 2023, **471**, 144463.
- 38 F. Jiang, S. Cui, N. Song, L. Shi and P. Ding, Hydrogen Bond-Regulated Boron Nitride Network Structures for Improved Thermal Conductive Property of Polyamide-Imide Composites, *ACS Appl. Mater. Interfaces*, 2018, **10**, 16812–16821.
- 39 K. Li, B. He, R. Wang, R. Yan, R. Zhang and R. Liu, Interfacial hydrogen bond effect between CeO<sub>2</sub> and g-C<sub>3</sub>N<sub>4</sub> boosts conversion to adipic acid from aerobic oxidation of cyclohexane, *Chem. Eng. J.*, 2024, **490**, 151829.
- 40 S. Yang, Y. Zhang, Y. Zhang, J. Deng, N. Chen, S. Xie, Y. Ma and Z. Wang, Designing Anti-Swelling Nanocellulose Separators with Stable and Fast Ion Transport Channels for Efficient Aqueous Zinc-Ion Batteries, *Adv. Funct. Mater.*, 2023, **33**, 2304280.
- 41 C. Prehal, A. Samojlov, M. Nachtnebel, L. Lovicar, M. Kriechbaum, H. Amenitsch and S. A. Freunberger, *In situ* small-angle X-ray scattering reveals solution phase discharge of Li-O<sub>2</sub> batteries with weakly solvating electrolytes, *Proc. Natl. Acad. Sci. U. S. A.*, 2021, **118**, e2021893118.
- 42 F. Zhang, J. Luo, J. Chen, H. Luo, M. Jiang, C. Yang, H. Zhang, J. Chen, A. Dong and J. Yang, Interfacial Assembly of Nanocrystals on Nanofibers with Strong Interaction for Electrocatalytic Nitrate Reduction, *Angew. Chem., Int. Ed.*, 2023, **62**, e202310383.
- 43 C. F. J. Francis, I. L. Kyratzis and A. S. Best, Lithium-Ion Battery Separators for Ionic-Liquid Electrolytes: A Review, *Adv. Mater.*, 2020, **32**, 1904205.
- 44 N. Mittal, A. Ojanguren, N. Cavasin, E. Lizundia and M. Niederberger, Transient Rechargeable Battery with a High Lithium Transport Number Cellulosic Separator, *Adv. Funct. Mater.*, 2021, **31**, 2101827.
- 45 K. Ho, Y. Liu, D. K. Hwang and H. Zarrin, Boron Nitride Nanosheet-Based Gel Polymer Electrolytes for Stable Lithium Metal Batteries, *ACS Appl. Nano Mater.*, 2024, **7**, 10829–10839.
- 46 H. Qin, W. Chen, W. Kuang, N. Hu, X. Zhang, H. Weng, H. Tang, D. Huang, J. Xu and H. He, A Nature-Inspired Separator with Water-Confined and Kinetics-Boosted Effects for Sustainable and High-Utilization Zn Metal Batteries, *Small*, 2023, **19**, 2300130.
- 47 M. Wang, Z. Dai, C. Yang, D. Xu, X. Zhang, L. Que, X. Zhang and J. Qin, Boosting de-solvation *via* halloysite nanotubes-cellulose composite separator for dendrite-free zinc anodes, *Mater. Today Energy*, 2024, **46**, 101736.
- 48 Y. Fang, X. Xie, B. Zhang, Y. Chai, B. Lu, M. Liu, J. Zhou and S. Liang, Regulating Zinc Deposition Behaviors by the Conditioner of PAN Separator for Zinc-Ion Batteries, *Adv. Funct. Mater.*, 2022, **32**, 2109671.
- 49 F. Neese, Software update: the ORCA program system, version 4.0, *Wiley Interdiscip. Rev.:Comput. Mol. Sci.*, 2018, **8**, e1327.
- 50 F. Neese, The ORCA program system, *Wiley Interdiscip. Rev.:Comput. Mol. Sci.*, 2012, **2**, 73–78.
- 51 F. Neese, F. Wennmo, U. Becker and C. Riplinger, The ORCA quantum chemistry program package, *J. Chem. Phys.*, 2020, 152.
- 52 H. Fu, L. Xiong, W. Han, M. Wang, Y. J. Kim, X. Li, W. Yang and G. Liu, Highly active crystal planes-oriented texture for reversible high-performance Zn metal batteries, *Energy Storage Mater.*, 2022, **51**, 550–558.
- 53 T. Wang, J. Sun, Y. Hua, B. N. V. Krishna, Q. Xi, W. Ai and J. S. Yu, Planar and dendrite-free zinc deposition enabled by exposed crystal plane optimization of zinc anode, *Energy Storage Mater.*, 2022, **53**, 273–304.
- 54 D. Xie, Z.-W. Wang, Z.-Y. Gu, W.-Y. Diao, F.-Y. Tao, C. Liu, H.-Z. Sun, X.-L. Wu, J.-W. Wang and J.-P. Zhang, Polymeric Molecular Design Towards Horizontal Zn Electrodeposits at Constrained 2D Zn<sup>2+</sup> Diffusion: Dendrite-Free Zn Anode for Long-Life and High-Rate Aqueous Zinc Metal Battery, *Adv. Funct. Mater.*, 2022, **32**, 2204066.
- 55 Z. Zhao, J. Zhao, Z. Hu, J. Li, J. Li, Y. Zhang, C. Wang and G. Cui, Long-life and deeply rechargeable aqueous Zn anodes enabled by a multifunctional brightener-inspired interphase, *Energy Environ. Sci.*, 2019, **12**, 1938–1949.
- 56 X. Li, Z. Chen, P. Ruan, X. Hu, B. Lu, X. Yuan, S. Tian and J. Zhou, Inducing preferential growth of the Zn (002) plane by using a multifunctional chelator for achieving highly reversible Zn anodes, *Nanoscale*, 2024, **16**, 2923–2930.
- 57 H. Peng, X. Wang, F. Yang, Z. Liu, H. Lei, S. Cui, X. Xie and G. Ma, Regulating solvation structure and inducing Zn (002) plane by a multifunctional electrolyte additive toward dendrite suppression and long-life zinc ion hybrid capacitors, *Chem. Eng. J.*, 2023, **474**, 145864.
- 58 F. Wu, F. Du, P. Ruan, G. Cai, Y. Chen, X. Yin, L. Ma, R. Yin, W. Shi, W. Liu, J. Zhou and X. Cao, Regulating zinc deposition behaviors by using a functional PANI modification layer on a separator for high performance aqueous zinc-ion batteries, *J. Mater. Chem. A*, 2023, **11**, 11254–11263.
- 59 X. Zhang, J. Li, D. Liu, M. Liu, T. Zhou, K. Qi, L. Shi, Y. Zhu and Y. Qian, Ultra-long-life and highly reversible Zn metal anodes enabled by a desolvation and deanionization interface layer, *Energy Environ. Sci.*, 2021, **14**, 3120–3129.

